Supporting Information for

Reduced Recombination and Capacitor-like Charge Buildup in an Organic Heterojunction

Authors: Kyra N. Schwarz[1,3], Paul B. Geraghty[2,3], Valerie D. Mitchell[2,3], Saeed-Uz-Zaman Khan[4], Oskar J. Sandberg[6], Nasim Zarrabi[6], Bryan Kudisch[1], Jegadesan Subbiah[2,3], Trevor A. Smith[3], Barry P. Rand[4,5], Ardalan Armin[6], Gregory D. Scholes[1,3]*, David J. Jones[2,3], Kenneth P. Ghiggino[3]*

[1]Department of Chemistry, Princeton University, Princeton, NJ 08544, USA

[2]Bio21 Institute and [3]School of Chemistry, University of Melbourne, Parkville, VIC 3010, Australia

[4]Department of Electrical Engineering and [5]Andlinger Center for Energy and the Environment, Princeton University, Princeton, NJ 08544, USA

[6]Department of Physics, Swansea University, Singleton Park, Swansea, SA2 8PP, Wales, United Kingdom

*Correspondence to: gscholes@princeton.edu and ghiggino@unimelb.edu.au

This PDF file includes:

Supplementary Text
Figs. S1 to S16
References

Supplementary Text

S1. Device Performance

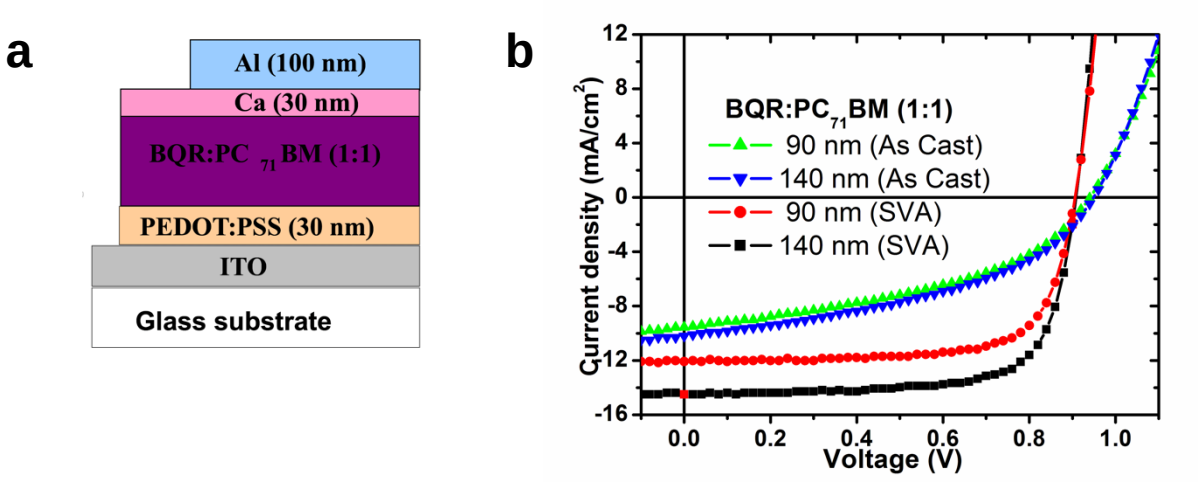

Figure- S1. | a Device architecture and **b** *J-V* curves for BQR:$PC_{71}BM$ devices of 90 nm and 140 nm thickness before and after solvent vapor annealing.

Table S1. | Photovoltaic performances of BQR:$PC_{71}BM$ bulk heterojunction solar cells fabricated with different annealing conditions and thicknesses.

BQR:$PC_{71}BM$ - Thickness	**J_{sc}(mA/cm^2)**	**V_{oc} (V)**	**FF (%)**	**PCE (%)**
90 nm (as-cast)	9.6	0.92	44	3.9
90 nm (SVA)	12.1	0.90	73	7.9
140 nm (as-cast)	10.1	0.92	45	4.2
140 nm (SVA)	14.5	0.90	72	9.6
320 nm (as-cast)	9.8	0.84	41	3.4
320 nm (SVA)	14.8	0.88	74	9.7
600 nm (as-cast)	8.5	0.89	39	2.9
600 nm (SVA)	15.3	0.88	61	8.1

S2. Bulk Heterojunction Morphology

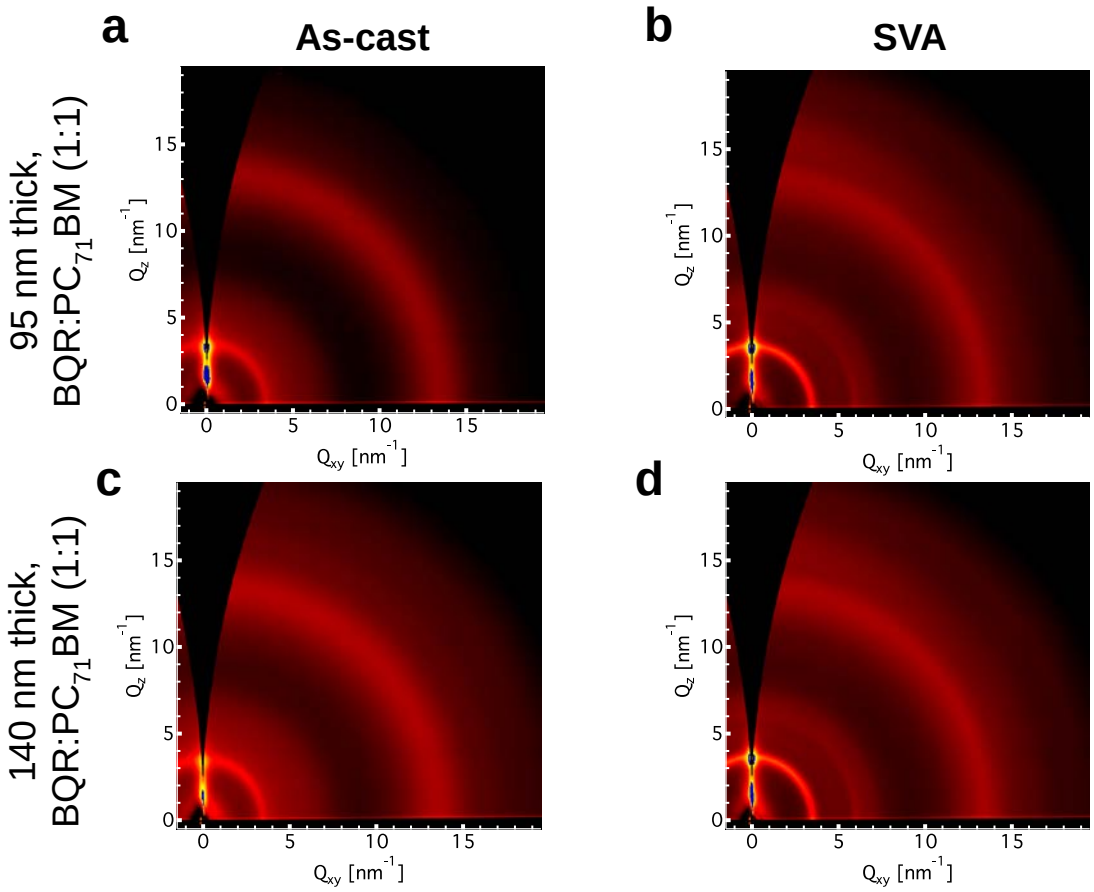

Figure- S2. | GIWAXS for BQR:$PC_{71}BM$ blend films of 95 nm thickness that are **a**, as-cast and **b**, solvent vapor annealed, and 140 nm blend films that are **c**, as-cast and, **d**, solvent vapor annealed.

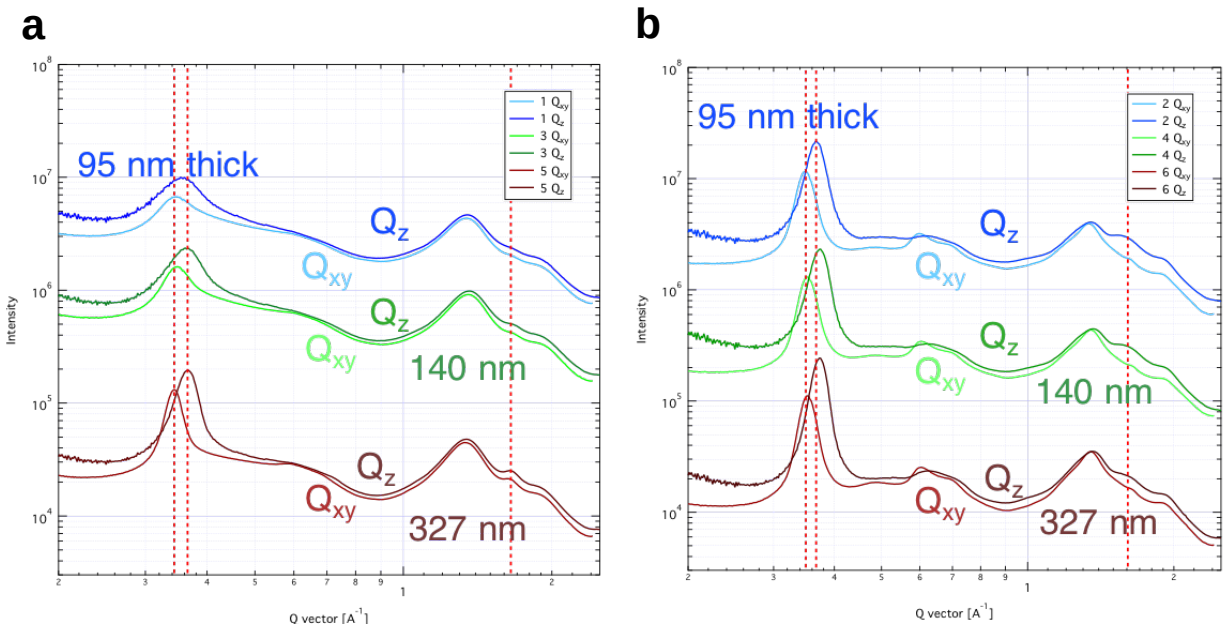

Figure S3 | GIWAXS line profiles in the Q_{xy} and Q_z directions for 95 nm, 140 nm and 327 nm thick BQR:$PC_{71}BM$ blend films **a,** as-cast and **b,** following solvent vapor annealing.

The aggregate development from as-cast to SVA films is independent of active layer thickness, shown optically with similar vibronic line shapes for the 95 nm and 140 nm thick samples (main text Fig. 1**b**), and in GIWAXS measurements (Figure S2**a**–**d** and S3**a**–**b**).

The key features of GIWAXS indicate that all films increase in crystallinity with SVA. The reflection at 1.58 $Å^{-1}$ is indicative of (010) BQR π–π stacking, with lamellar stacking of BQR indicated by (100) peaks at 0.65 $Å^{-1}$(Fig. S1). Both of these features increase after solvent vapor annealing, more clearly visualized in the line profiles in Figure S3 **a** and **b**. This increase with SVA of the (100) reflection is predominantly along the Q_{xy} axis, indicating that crystallites are slightly anisotropic with more π-stacking of molecules in the face-on direction, parallel to the substrate. The stronger tendency to take face-on orientation is generally associated with more favorable transport properties, leading to enhanced J_{sc} and fill factors, and better photoconversion efficiency[1]. A broad 1.3 $Å^{-1}$ peak indicates the presence of amorphous $PC_{71}BM$ aggregates. With SVA, this peak sharpens/narrows indicating an increase in aggregation and slight introduction of crystallinity.

Application of Scherrer analysis to Gaussian fits of the 0.35 A^{-1} peak corresponding to alkyl lamella yields average crystallite correlation lengths (CCLs) for as-cast films of 10.39 nm (95 nm film) and 12.48 nm (140 nm film). SVA films had larger CCLs of 18.05 nm (95 nm film) and 18.81 nm (140 nm film).

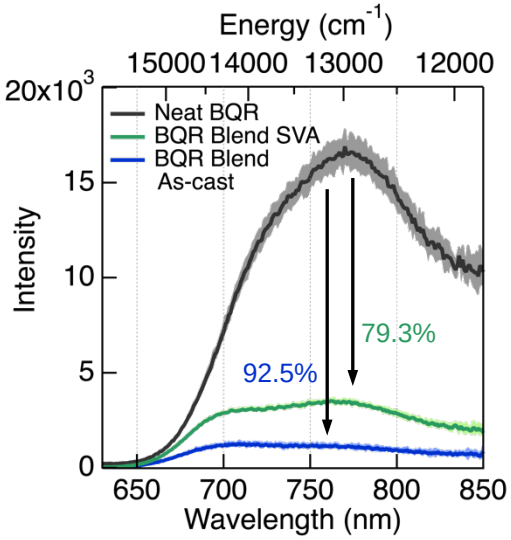

Figure S4. | BQR exciton fluorescence of films excited at 600 nm, of neat BQR (grey), 1:1 BQR:$PC_{71}BM$ blend films as-cast (blue) and after undergoing SVA treatment (green) indicating the quenching of BQR exciton emission due to charge transfer. As-cast blends have exciton quenching of 92.5 % compared to 79.3 % for SVA blends which have more pure BQR domains. The shaded area surrounding each trace indicates the standard deviation of ten measurements.

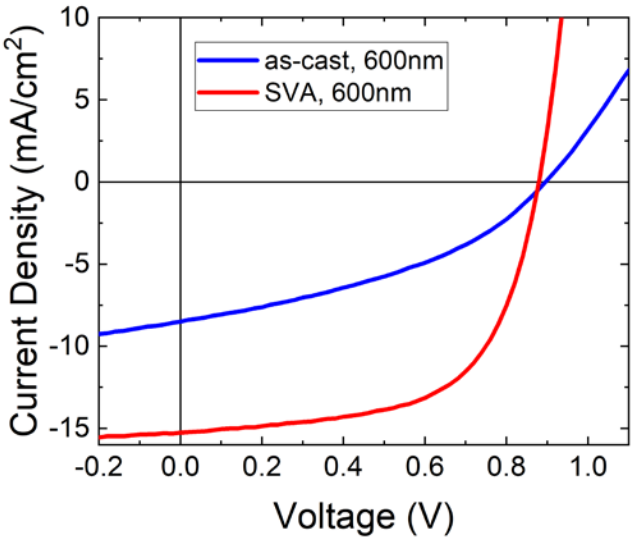

Figure S5. | Measured current-voltage characteristics under AM1.5 incident light intensity of 600 nm thick as-cast (blue) and SVA devices (red). The corresponding solar cell parameters for the as-cast device read: PCE = 2.95%, FF = 38.8%, J_{sc} = 8.49 mA/cm^2 and V_{oc} = 0.89 V; whereas for the SVA device: PCE = 8.14%, FF = 60.7%, J_{sc} = 15.25 mA/cm^2, and V_{oc} = 0.879 V.

Table S2. | Parameters used in the electro-optical device simulations (see Figure 2**a** and 2**c**).

Parameter	**as-cast**	**SVA**
Active layer thickness, d (nm)	320	320
Temperature, T (K)	300	300
Relative permittivity, ε	4.2	4.2
Electron mobility, μ_n (cm^2/Vs)	1.5×10^{-3}	3×10^{-3}
Hole mobility, μ_p (cm^2/Vs)	4×10^{-5}	8×10^{-4}
Recombination reduction factor, γ	0.07	0.0005
Electrical bandgap, E_g (eV)	1.32	1.32
Effective density of states, N_0 (cm^{-3})	10^{20}	10^{20}
Built-in voltage, V_{bi} (V)	1.1	1.1
Hole injection barrier at anode (eV)	0.02	0.02
Electron injection barrier at cathode (eV)	0.20	0.20

S3. Transient Absorption Measurements

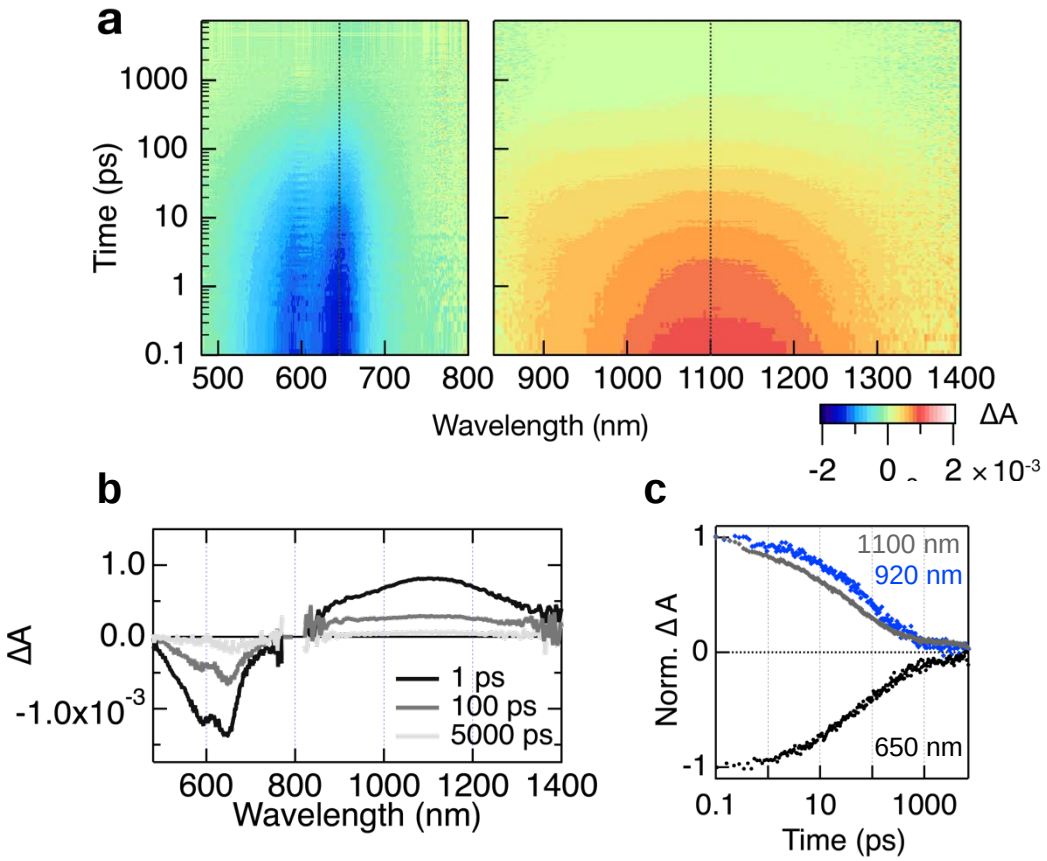

Figure S6 | a, Time-resolved transient absorption of a neat BQR film, with 600 nm excitation at 2.5 μJ/cm^2. **b,** Spectral slices at 1 ps, 100 ps and 5000 ps of the neat BQR film, and **c,** Normalized dynamics at 650 nm of the ground state bleach, and at 920 nm and 1100 nm of the excited state absorption of the photoexcited exciton state, indicating that the primary decay pathway is the lifetime of the BQR exciton.

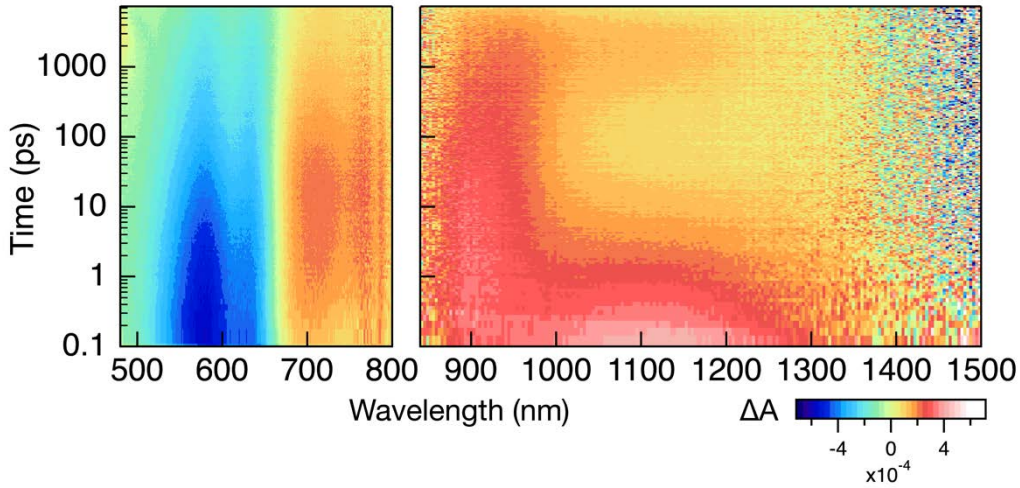

Figure S7 | Time-resolved transient absorption of 95 nm thick BQR:$PC_{71}BM$ film as-cast, with 600 nm excitation at 2.5 μJ/cm^2. We note that the raw kinetic slices at 920 nm (main text Fig. 3**e**) at later times can be obscured by spectral shifts and overlap with other species, and therefore are no longer a clear representation of the polaron PIA dynamics.

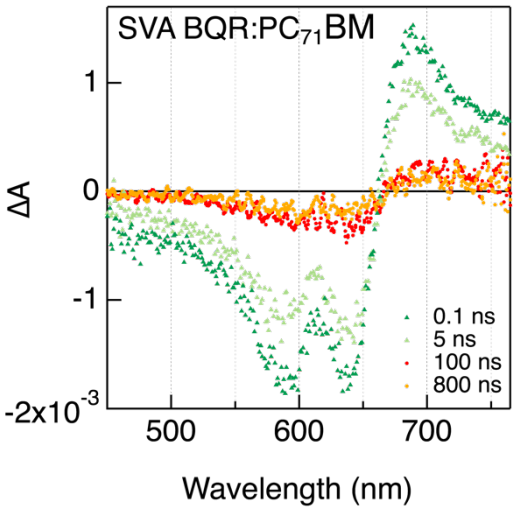

Figure S8 | Transient absorption of 140 nm thick BQR:$PC_{71}BM$ film after solvent vapor annealing, with 600 nm excitation at 10 μJ/cm^2 (due to limitations in data quality for long time delays). Spectra are taken at 0.1 ns and 5 ns using a physical delay stage, and 100 ns and 800 ns using an electronic delay (see methods for details). The second derivative signature of the EA does not appear to be prominent in the data ≥100 ns delay.

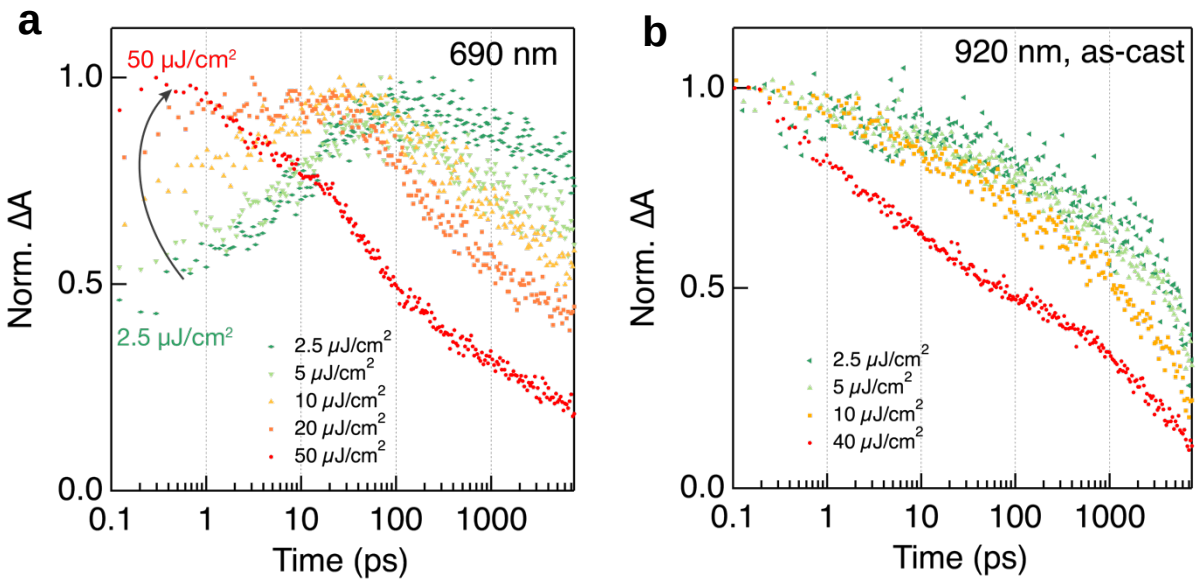

Figure S9 | Power dependence of transient absorption dynamics **a**, at 690 nm (predominantly the electro-absorption signal) of a 140 nm thick BQR:$PC_{71}BM$ film after solvent vapor annealing (as shown in Figure 3**c**) and **b**, at 920nm (polaron) of a 140 nm thick BQR:$PC_{71}BM$ as-cast film, showing a clear power dependence. The film was excited with a 600 nm pump pulse at 2.5, 5, 10, 20 and 50 μJ/cm^2.

S4. The Stark Effect in Organic Photovoltaic Blends

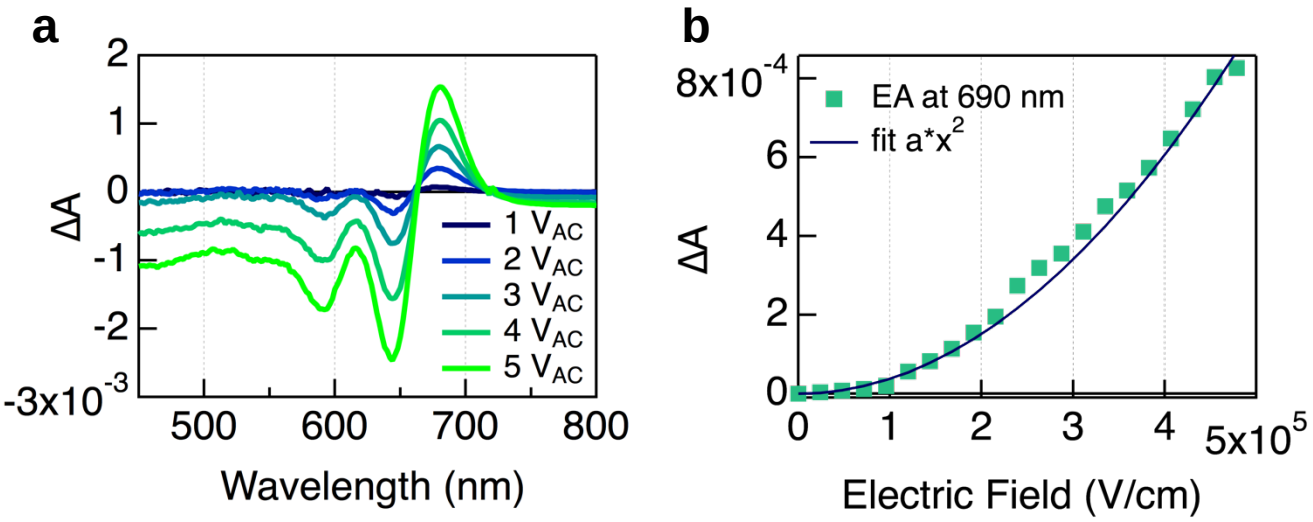

Figure S10 | a, Steady-state electro-absorption of a BQR:$PC_{71}BM$ device under an applied AC voltage of 1–5 V, with a constant offset of -1 V DC to avoid charge injection. **b,** Electro-absorption at 690 nm (peak amplitude) as a function of applied AC bias. The AC voltage was converted to electric field by dividing by the device thickness in cm, here 83.6×10^{-7} cm. The prefactor, *a*, in the quadratic fit is 3.79×10^{-15}.

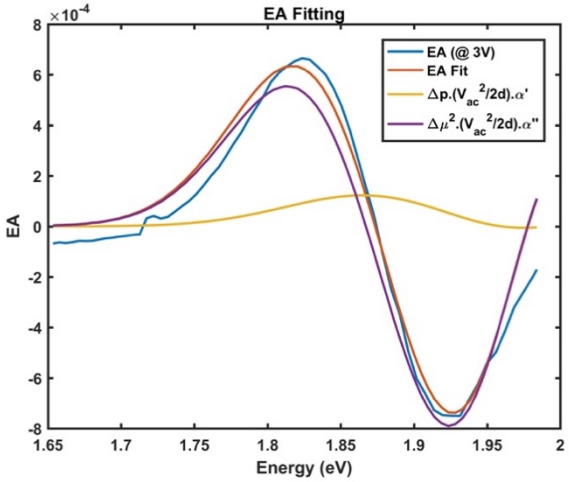

Figure S11 | a, Steady-state electro-absorption of a BQR:$PC_{71}BM$ device under an applied AC voltage of 3 V, with a constant offset of -1 V DC to avoid charge injection. The change in dipole moment and change in polarizability extraction from the steady-state electro-absorption signal. Fitting the EA signal from 630 nm–750 nm, change in polarizability, Δp = 35.38 $Å^3$, change in

dipole, $\Delta\mu$ = 8.43 D. This Δp is quite small and the electro-absorption can be fitted almost entirely with the second derivative of the absorption coefficient.

The Stark effect describes the effect of an electric field on the absorption or emission of an absorbing species. When arising from intrinsically generated charges, it has been broadly used as a probe of nanoscale excited-state processes involving charged species that generate an electric field between them[2–4]. This is different to the case of Stark spectroscopy, where the electric field in question is macroscopic, and deliberately applied across a sample with electrodes[5–7].

The change in transition frequency, Δv, of a molecular transition due to an electric field, $\vec{F}$, is given by:

$$\Delta v = -\Delta\vec{\mu} \cdot \vec{F} - 1/2\vec{F} \cdot \Delta\alpha \cdot \vec{F}$$

where $\Delta\vec{\mu}$ is the change in dipole moment and $\Delta\alpha$ is the change in polarizability resulting from the electric field[8].

The linear Stark effect results from a change in dipole moment, $\Delta\vec{\mu}$, where the effect of an electric field on molecular energy levels is a function of the field's angle with respect to the transition dipole moment of the affected absorbers[4]. For Stark spectroscopy of an isotropic, immobilized sample, the molecular dipoles are at many different orientations with respect to the externally applied field, which shifts the transitions to both higher and lower transition energies; the difference spectrum resulting in a second derivative lineshape. This is the case in Figure S10**a**, and is also the case for photogenerated charges that cause an intrinsic electro-absorption in a sample where the field and molecules are at many relative orientations to one another (as described in the main text, Figure 4**a**-**b**)[9].

The quadratic Stark shift results from a change in polarizability, $\Delta\alpha$. The molecular polarizability change interacts with the field to induce a dipole moment only in one direction, typically in the direction of the applied field, regardless of the molecule's orientation. This results in a first derivative lineshape, regardless of the whether the electric field is applied macroscopically or is intrinsic within a sample[8,9].

Throughout this work, we exclusively observe the excitonic, electro-absorption signature of the donor BQR. This is in contrast to the sub-bandgap charge transfer state electro-absorption signals that can also be observed in Stark spectroscopies of bulk heterojunctions[10,11].

Figure S10**a** shows Stark spectroscopy of a BQR:$PC_{71}BM$ device. We see a second derivative lineshape for the electro-absorption indicating that the Stark effect originates from a change in dipole moment, $\Delta\mu$, of an isotropic BQR sample. This is consistent with the EA observed in transient absorption spectra that are due to photogenerated free charges where the orientations of BQR molecules and the electric fields are at many different relative orientations.

In Figure S10**b** the quadratic dependence of EA intensity on voltage is observed in isotropic samples due to orientational averaging, consistent with the linear Stark effect observed in an isotropic sample[8]. This dependence allows us to calibrate the electro-absorption signal observed in transient measurements against the steady-state electro-absorption spectra for BQR:$PC_{71}BM$ devices. Fitting a second order polynomial for an electric field in V/cm gives a quadratic prefactor value of 3.79×10^{-15} for BQR. The EA signal is equal to $\int\left|\vec{E}\right|^2 dV$ multiplied by this prefactor, where is $\vec{E}$ is the electric field in V/cm, and dV is the volume element.

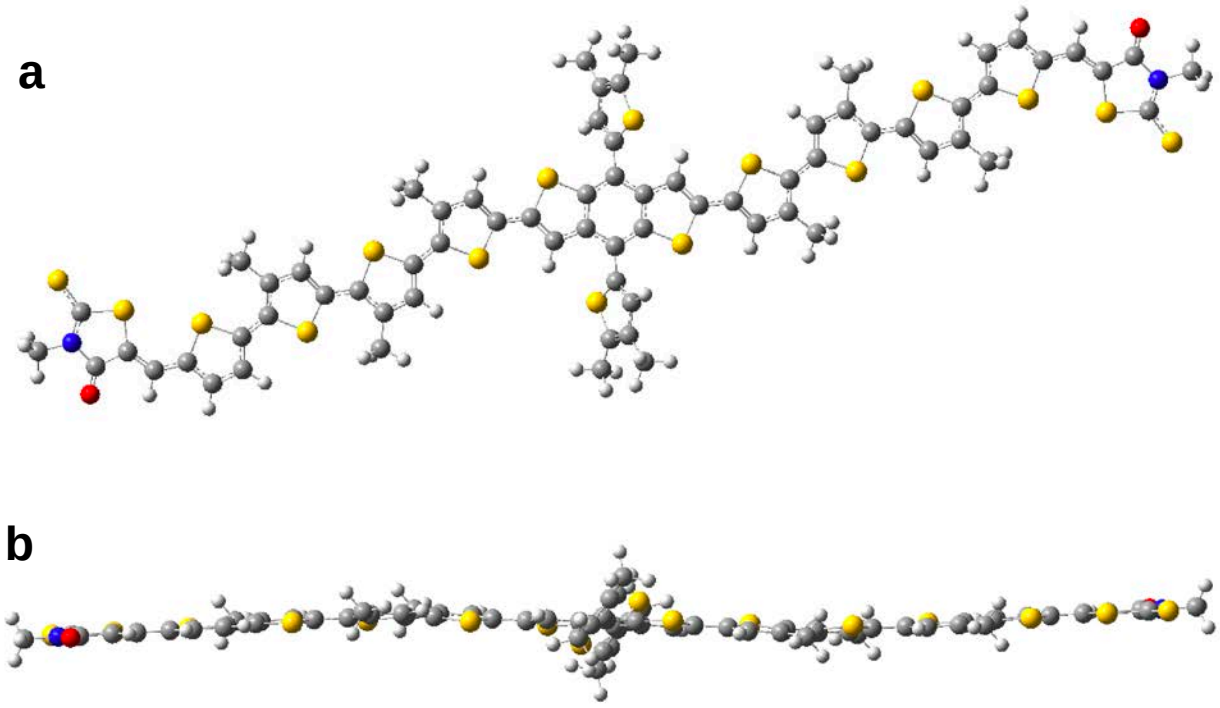

Figure S12 | Optimized ground state geometry of BQR calculated with density functional theory (DFT) calculations performed using B3LYP 6-31G(d,p) functional and basis set. **a,** top view and **b,** side view.

S5. Transient Absorption Spectral Extraction Using a Genetic Algorithm

The method of spectral extraction for transient absorption data using a genetic algorithm is presented in reference[12] and is described in detail elsewhere[13,14].

This method has no fixed kinetic model with exponential rates, which can be relevant in thin film heterojunctions where a range of different morphological environments for chromophores can complicate the assignment of the dynamics using exponential rates. This method assumes that each spectral component, n, comprising the data has a fixed spectrum of the i^{th} component $S_i(\lambda)$ whose amplitude changes over time, $A_i(t)$. The transient absorption data can then be represented as:

$$\Delta A(\lambda, t) = \sum_{i=1}^{n} S_i(\lambda)\, A_i(t)$$

The optimal solution can be found using a genetic algorithm where a large population of solutions are initially generated and evaluated for their fitness. Solutions of a higher fitness are preferably selected and preserved when a new generation begins. A minimum of three spectral species was needed to describe the data for BQR:$PC_{71}BM$ blend films. An initial guess for one species used the spectrum of neat BQR to describe the BQR exciton, and a second used the BQR hole polaron spectrum, which was constant held during the fit.

The extracted signals for 140 nm thick SVA BQR:$PC_{71}BM$ films, shown in Fig. 3**c** in the main text, resemble the spectra of the BQR exciton, BQR hole polaron and second derivative EA of the ground-state absorption of the blend. We note that the extracted EA signal, while largely described by the second derivative of the ground state absorption, also captures a shifting feature of the polaron PIA at ~950 nm. This is because the global analysis method used here does not successfully capture spectral shifts, and the hole relaxation is occurring on the same timescale as the EA grow-in. Here, a red-shift in the transient signal maximum corresponds to the relaxation of BQR charges from higher energy disordered sites to lower energy ordered aggregates where charges can pool in higher densities.

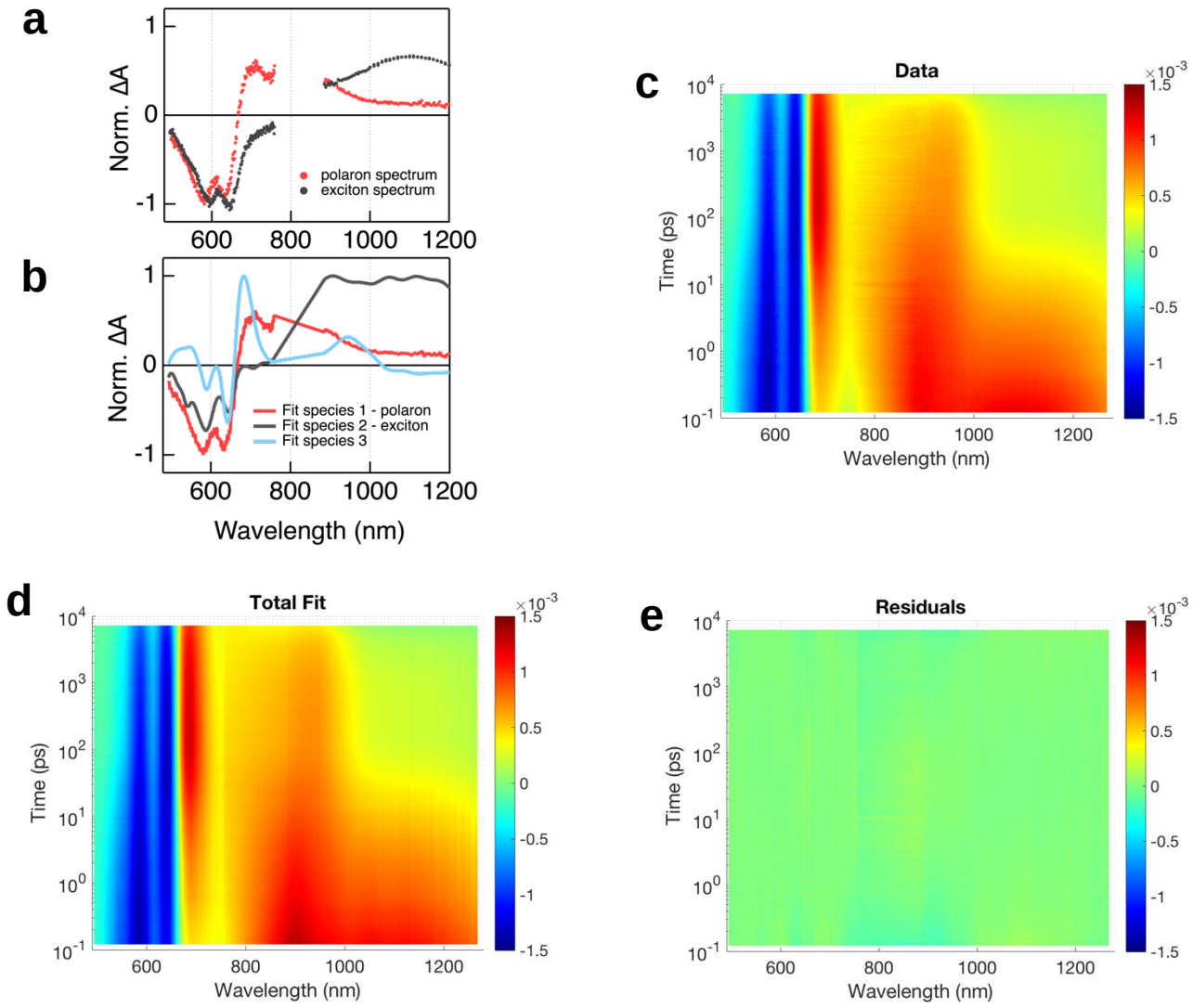

Figure S13 | a, Inputs for fitting with the genetic algorithm described above. The polaron spectrum is input as a fixed component, from blend data where the polaron is the only component at late times after exciton decay. The exciton component is input as a starting guess for the second component, taken from the neat BQR transient absorption at 1ps. **b,** Outputs from the genetic algorithm fit. Two components do not adequately fit the data, however, three components are able to reproduce the data surface. The third component is allowed to float within the fit, and after the fit resembles the device EA. **c,** Transient absorption data surface for 140nm SVA films for fitting and **d,** fit surface from the genetic algorithm using the three components as described above. **e,** Residuals from the fit in **d.**

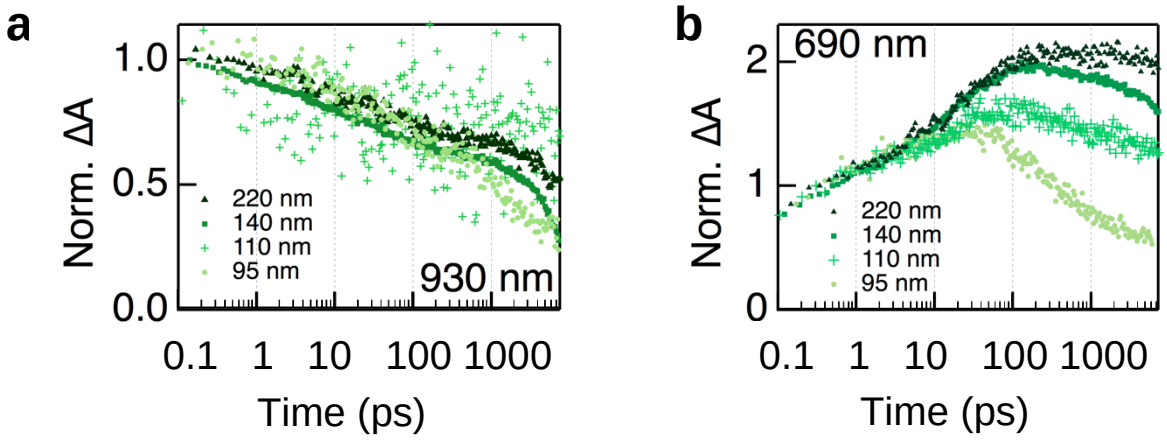

Figure S14 | Thickness dependence of transient absorption dynamics at **a,** 930 nm (polaron signal) and at **b,** 690 nm (predominately the electro-absorption signal) of BQR:$PC_{71}BM$ films after solvent vapor annealing. The film was excited with 600 nm pump pulse at 2.5 μJ/cm^2. While thickness may have a small effect on the recombination dynamics (i.e the polaron signal) of films of different optical density, the thickness dependence of the EA signal at 690 nm is quite significant.

S6. Triplet Exciton Generation in As-cast BQR Blends

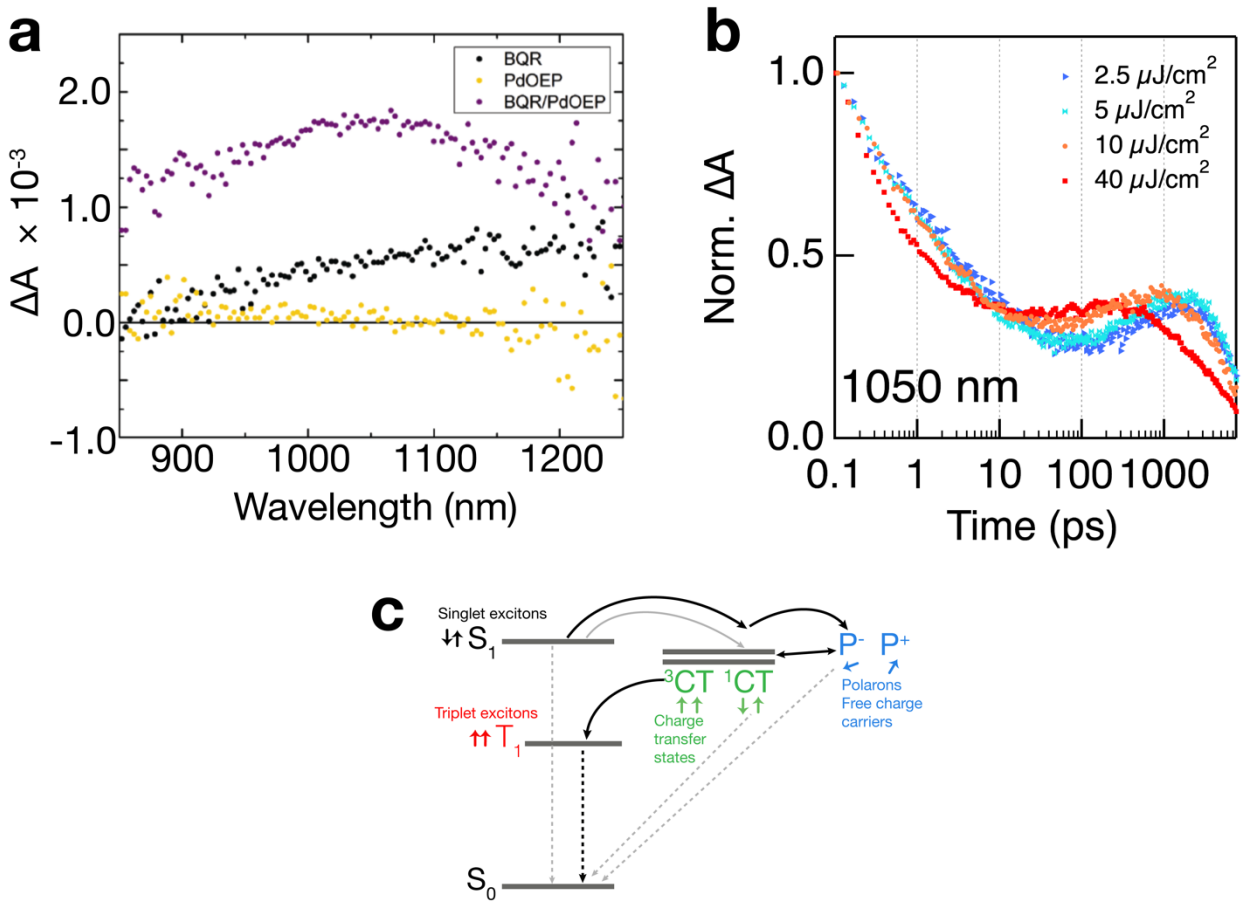

Figure S15 | a, The BQR triplet exciton spectrum obtained using triplet sensitizer PdOEP (purple) blended in a BQR:PdOEP, 1:1 wt.% film. Films were excited at 553 nm (the absorption maximum of PdOEP films) at 830 ps delay. Neat films of BQR (black dots) and PdOEP (yellow dots) are also shown for comparison at 830 nm under the same excitation conditions. The pump excitation intensity was 7 μJ/cm^2 for all samples. **b,** Pump power dependence of triplet generation, where the intensity dependent triplet growth infers that free carriers are influence triplet generation. **c,** An energy level diagram of charge generation and recombination pathways in a bulk heterojunction, emphasizing the pathway of triplet exciton generation *via* spin-uncorrelated free polarons.

The generation of the BQR triplet exciton spectrum in blend films (Fig. S15**a**) has a significant power dependence (Fig. S15**b**), having formed from a bimolecular rather than a geminate recombination pathway. This triplet loss pathway is significant and equivalent for as-cast heterojunctions in both thick (Fig. 3**a**) and thin films (Fig. S7). Following charge separation, free polarons can recombine to form singlet and triplet CT states in the ratio of 1:3 as dictated by spin statistics. Triplet CT states can then go on to form triplet exciton states on the donor if energetically accessible (Fig S15**c**)[15]. Recent work also suggests that smaller donor-acceptor separations can increase back transfer from the CT state to the lower energy localized triplet state.[16]

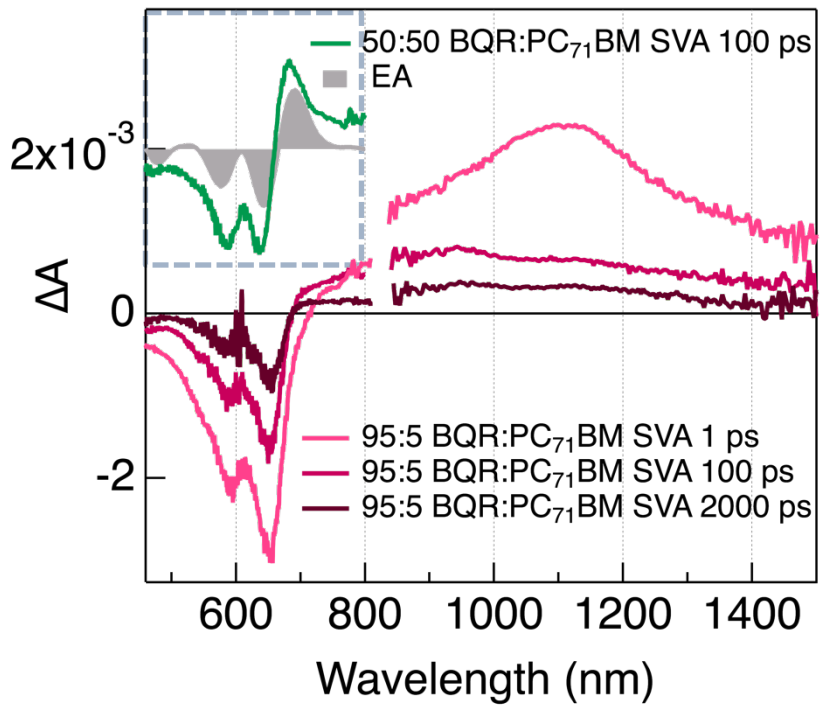

Figure S16 | Transient dynamics of a 95:5 BQR:PC_{71}BM SVA film also showing the visible portion of the 50:50 BQR:PC_{71}BM SVA film and device electro-absorption (inset), vertically offset for comparison. In the 95:5 BQR:PC_{71}BM blend, excitons undergo charge separation to form polarons. However, unlike the 50:50 SVA blend, we see no evidence of charge buildup or capacitive charging due to the absence of a morphological cascade.

References

(1) Kim, Y. J.; Song, C. E.; Suranagi, S. R.; Lee, J. C.; Park, C. E. Markedly Different Molecular Formation in DPP-Based Small-Molecule Solar Cells Probed by Grazing-Incidence Wide-Angle X-Ray Scattering. *Acta Crystallogr. Sect. B Struct. Sci. Cryst. Eng. Mater.* **2017**, *73*, 916–922. https://doi.org/10.1107/S2052520617009933.

(2) Klimov, V. I. Spectral and Dynamical Properties of Multiexcitons in Semiconductor Nanocrystals. *Annu. Rev. Phys. Chem.* **2007**, *58*, 635–673. https://doi.org/10.1146/annurev.physchem.58.032806.104537.

(3) Ardo, S.; Sun, Y.; Castellano, F. N.; Meyer, G. J. Excited-State Electron Transfer from Ruthenium-Polypyridyl Compounds to Anatase TiO2 Nanocrystallites: Evidence for a Stark Effect. *J. Phys. Chem. B* **2010**, *114* (45).

(4) Koch, M.; Myahkostupov, M.; Oblinsky, D. G.; Wang, S.; Garakyaraghi, S.; Castellano, F. N.; Scholes, G. D. Charge Localization after Ultrafast Photoexcitation of a Rigid Perylene Perylenediimide Dyad Visualized by Transient Stark Effect. *J. Am. Chem. Soc.* **2017**, *139* (15), 5530–5537. https://doi.org/10.1021/jacs.7b01630.

(5) Cabanillas-Gonzalez, J.; Virgili, T.; Gambetta, A.; Lanzani, G.; Anthopoulos, T. D.; De Leeuw, D. M. Photoinduced Transient Stark Spectroscopy in Organic Semiconductors: A Method for Charge Mobility Determination in the Picosecond Regime. *Phys. Rev. Lett.* **2006**, *96* (10), 6–9. https://doi.org/10.1103/PhysRevLett.96.106601.

(6) Vithanage, D. A.; Devižis, A.; Abramavičius, V.; Infahsaeng, Y.; Abramavičius, D.; MacKenzie, R. C. I.; Keivanidis, P. E.; Yartsev, A.; Hertel, D.; Nelson, J.; Sundström, V.; Gulbinas, V. Visualizing Charge Separation in Bulk Heterojunction Organic Solar Cells. *Nat. Commun.* **2013**, *4* (1), 2334. https://doi.org/10.1038/ncomms3334.

(7) Devižis, A.; Hertel, D.; Meerholz, K.; Gulbinas, V.; Moser, J.-E. Time-Independent, High Electron Mobility in Thin PC61BM Films: Relevance to Organic Photovoltaics. *Org. Electron.* **2014**, *15* (12), 3729–3734. https://doi.org/https://doi.org/10.1016/j.orgel.2014.10.028.

(8) Boxer, S. Stark Realities. *J. Phys. Chem. B* **2009**, *112* (41), 592–602.

(9) Bublitz, G.; Boxer, S. Stark Spectroscopy: Applications in Chemistry, Biology, and Materials Science. *Annu. Rev. Phys. Chem.* **1997**, *48*, 213–242. https://doi.org/10.1146/annurev.physchem.48.1.213.

(10) Tsang, S. W.; Chen, S.; So, F. Energy Level Alignment and Sub-Bandgap Charge Generation in Polymer:Fullerene Bulk Heterojunction Solar Cells. *Adv. Mater.* **2013**, *25* (17), 2434–2439. https://doi.org/10.1002/adma.201204495.

(11) Bernardo, B.; Cheyns, D.; Verreet, B.; Schaller, R. D.; Rand, B. P.; Giebink, N. C.

Delocalization and Dielectric Screening of Charge Transfer States in Organic Photovoltaic Cells. *Nat. Commun.* **2014**, *5*, 1–7. https://doi.org/10.1038/ncomms4245.

(12) Gélinas, S.; Paré-Labrosse, O.; Brosseau, C.-N.; Albert-Seifried, S.; McNeill, C. R.; Kirov, K. R.; Howard, I. a; Leonelli, R.; Friend, R. H.; Silva, C. The Binding Energy of Charge-Transfer Excitons Localized at Polymeric Semiconductor Heterojunctions. *J. Phys. Chem. C* **2011**, *115* (14), 7114–7119.

(13) Chow, P. C. Y.; Gélinas, S.; Rao, A.; Friend, R. H. Quantitative Bimolecular Recombination in Organic Photovoltaics through Triplet Exciton Formation. *J. Am. Chem. Soc.* **2014**, *136* (9), 3424–3429. https://doi.org/10.1021/ja410092n.

(14) Gelinas, S.; Rao, A.; Kumar, A.; Smith, S. L.; Chin, A. W.; Clark, J.; van der Poll, T. S.; Bazan, G. C.; Friend, R. H. Ultrafast Long-Range Charge Separation in Organic Semiconductor Photovoltaic Diodes. *Science* **2014**, *343* (6170), 512–516. https://doi.org/10.1126/science.1246249.

(15) Rao, A.; Chow, P. C. Y.; Gélinas, S.; Schlenker, C. W.; Li, C. Z.; Yip, H. L.; Jen, A. K. Y.; Ginger, D. S.; Friend, R. H. The Role of Spin in the Kinetic Control of Recombination in Organic Photovoltaics. *Nature* **2013**, *500* (7463), 435–439. https://doi.org/10.1038/nature12339.

(16) Chang, W.; Congreve, D. N.; Hontz, E.; Bahlke, M. E.; McMahon, D. P.; Reineke, S.; Wu, T. C.; Bulović, V.; Van Voorhis, T.; Baldo, M. A. Spin-Dependent Charge Transfer State Design Rules in Organic Photovoltaics. *Nat. Commun.* **2015**, *6*, 1–6. https://doi.org/10.1038/ncomms7415.